

MEASURING ALIGNMENTS BETWEEN GALAXIES AND THE COSMIC WEB AT $z \sim 2 - 3$ USING IGM TOMOGRAPHY

ALEX KROLEWSKI¹, KHEE-GAN LEE^{2,4}, ZARIJA LUKIĆ², MARTIN WHITE^{1,2,3}

¹Department of Astronomy, University of California at Berkeley, New Campbell Hall, Berkeley, CA 94720, USA

²Lawrence Berkeley National Lab, 1 Cyclotron Road, Berkeley, CA 94720, USA

³Department of Physics, University of California at Berkeley, Le Conte Hall, Berkeley, CA 94720, USA

⁴Hubble Fellow

ABSTRACT

Many galaxy formation models predict alignments between galaxy spin and the cosmic web (i.e. the directions of filaments and sheets), leading to intrinsic alignment between galaxies that creates a systematic error in weak lensing measurements. These effects are often predicted to be stronger at high-redshifts ($z \gtrsim 1$) that are inaccessible to massive galaxy surveys on foreseeable instrumentation, but IGM tomography of the Ly α forest from closely-spaced quasars and galaxies is starting to measure the $z \sim 2 - 3$ cosmic web with the requisite fidelity. Using mock surveys from hydrodynamical simulations, we examine the utility of this technique, in conjunction with coeval galaxy samples, to measure alignment between galaxies and the cosmic web at $z \sim 2.5$. We show that IGM tomography surveys with $\lesssim 5 h^{-1}$ Mpc sightline spacing can accurately recover the eigenvectors of the tidal tensor, which we use to define the directions of the cosmic web. For galaxy spins and shapes, we use a model parametrized by the alignment strength, $\Delta\langle\cos\theta\rangle$, with respect to the tidal tensor eigenvectors from the underlying density field, and also consider observational effects such as errors in the galaxy position angle, inclination, and redshift. Measurements using the upcoming $\sim 1 \text{ deg}^2$ CLAMATO tomographic survey and 600 coeval zCOSMOS-Deep galaxies should place 3σ limits on extreme alignment models with $\Delta\langle\cos\theta\rangle \sim 0.1$, but much larger surveys encompassing $> 10,000$ galaxies, such as Subaru PFS, will be required to constrain models with $\Delta\langle\cos\theta\rangle \sim 0.03$. These measurements will constrain models of galaxy-cosmic web alignment and test tidal torque theory at $z \sim 2$, improving our understanding of the redshift dependence of galaxy-cosmic web alignment and the physics of intrinsic alignments.

Keywords: keywords: cosmology: observations — galaxies: high-redshift — intergalactic medium — quasars: absorption lines — large-scale structure of universe

1. INTRODUCTION

Gravitational collapse of the Gaussian random-phase initial conditions produced by inflation creates a network of dense nodes connected by filaments and sheets and separated by voids, the “cosmic web” (Zeldovich et al. 1982; Klypin & Shandarin 1983; Einasto et al. 1984; Davis et al. 1985; Geller & Huchra 1989; Bond et al. 1996). As a result of nonlinear structure formation, the cosmic web is distinctly non-Gaussian. In the Zel’dovich approximation, collapse occurs sequentially along the principal axes of the deformation tensor, as matter flows out of voids onto sheets, collapses into filaments and finally streams into high-density nodes (Zel’dovich 1970). The accretion of matter determines the shapes and angular momenta of galaxies and their host dark matter halos, naturally suggesting a connection between the cosmic web and galaxy shapes and spins.

In the linear regime, the evolution of the angular momentum of a protohalo is described by tidal torque theory (TTT, Peebles 1969; Doroshkevich 1970; White 1984). TTT pre-

dicts that the protohalo’s angular momentum will be aligned with the intermediate eigenvector of the tidal tensor. However, nonlinear evolution can significantly weaken this alignment (Porciani et al. 2002), driving alignments with other preferred directions (e.g. the direction of filaments, along which matter is accreting; Codis et al. 2012)

Alignments between the cosmic web and halo shapes and spins have been extensively studied in N-body simulations (Kießling et al. 2015; see Tables 1 and 2 in Forero-Romero et al. (2014) for a recent compilation of results). Many workers suggest that halo spins transition from parallel to filaments at low halo mass to perpendicular to filaments at high mass (Aragón-Calvo et al. 2007, Hahn et al. 2007a, Codis et al. 2012, Trowland et al. 2013, Aragon-Calvo & Yang 2014). In addition, Dubois et al. (2014) and Codis et al. (2015), using the cosmological hydrodynamical simulation HorizonAGN, argue that galaxy spin alignments exhibit a similar transition mass. However, these results are dependent on the measurement algorithm, simulation, and environmental classification (Kießling et al. 2015), and it is unclear if spin-filament alignments are the dominant spin-cosmic web alignment. For instance, Libeskind et al. (2013) find a simi-

lar transition from aligned to anti-aligned in voids and sheets as well as filaments, although with a different transition mass in each web type, and Forero-Romero et al. (2014) find no alignment at low mass and argue that sheet alignments are as significant as filament alignments at high mass. In direct contradiction to the picture described above, the cosmological zoom simulations of Hahn et al. (2010) suggest that massive disk galaxies have spins parallel to their host filaments while low-mass disk galaxies have spins aligned along the intermediate axis of the tidal tensor.

In contrast, halo shape-cosmic web alignments are both stronger and more robust to measure than spin-cosmic web alignments (Kiessling et al. 2015), although they have been less extensively studied. The major axis of the halo inertia tensor is preferentially aligned along filaments, in the plane of sheets (Altay et al. 2006, Hahn et al. 2007a, Aragón-Calvo et al. 2007, Zhang et al. 2009, Libeskind et al. 2013, Forero-Romero et al. 2014) and parallel to the surface of voids (i.e. the plane of sheets; Patiri et al. 2006, Brunino et al. 2007, Cuesta et al. 2008). Shape-cosmic web alignments monotonically increase from weak to strong as a function of mass, with no transition mass (Hahn et al. 2007a, Aragón-Calvo et al. 2007, Zhang et al. 2009, Libeskind et al. 2013, Forero-Romero et al. 2014). Using the MassiveBlack-II cosmological hydrodynamical simulation, Chen et al. (2015) report similar results for alignments between galaxy shapes and filaments. Galaxy shape-cosmic web alignments are closely related to ellipticity-tidal shear correlations (Codis et al. 2015), the “GI” term of intrinsic alignments that is a potential major systematic for upcoming missions such as LSST, WFIRST and EUCLID that aim to measure the dark energy equation of state using weak lensing tomography (Hirata & Seljak 2004, Bridle & King 2007, Kirk et al. 2012).

Observational studies of galaxy-cosmic web alignment require large numbers of galaxy redshifts to trace the cosmic web in 3D, and are therefore primarily feasible only at low redshift. Observations of alignments between spiral galaxy spin and void surfaces/sheets have produced conflicting results ranging from parallel to random to perpendicular alignment (Trujillo et al. 2006, Slosar & White 2009, Varela et al. 2012). Locally, Navarro et al. (2004) find that spiral galaxy spins preferentially lie in the supergalactic plane. Early observations reported that spiral galaxy spins are aligned with the intermediate axis of the tidal shear tensor in concordance with TTT predictions (Lee & Pen 2002, Lee & Erdogdu 2007), and are therefore aligned perpendicular to filaments (Jones et al. 2010, Zhang et al. 2015). However, more recently Tempel et al. (2013) and Tempel & Libeskind (2013) have found that spiral galaxy spins are parallel to filaments and lenticular/elliptical galaxy spins are perpendicular to filaments, in concordance with the transition mass picture from simulations. Similarly, Pahwa et al. (2016) find that elliptical galaxy spins lie perpendicular to filaments and normal to sheets, while spiral galaxy spins exhibit much weaker alignments along filaments. In accordance with shape-cosmic web alignments from simulations, Zhang et al. (2013) find that galaxy major axes preferentially align with filaments and along sheets, a relationship that is weak for blue galaxies and

highly significant for bright red galaxies.

Similar measurements at higher redshift ($z > 0.5$) are challenging due to the difficulty of measuring the cosmic web from the galaxy distribution, requiring large samples of faint galaxies to achieve sufficient spatial resolution of a few Mpc, although surveys such as VIPERS (Guzzo et al. 2014, Malavasi et al. 2016) are pushing this to $z \sim 0.7$. Even with future 30m-class telescopes, it would be extremely time-consuming to obtain the requisite galaxy samples at $z > 1$ due to the high number densities required.

At higher redshifts, Lyman- α forest tomography (Pichon et al. 2001, Caucci et al. 2008) offers an alternative method for characterizing the cosmic web at $z \sim 2$, the epoch of peak star formation, by using observations of Ly α forest absorption in closely-spaced quasars and Lyman-break galaxies to reconstruct the IGM absorption field. Using this technique, current instrumentation can probe a spatial resolution of a few Mpc (Lee et al. 2016), similar to the resolution of cosmic web studies at $z < 0.5$ (c.f. the GAMA Survey; Eardley et al. 2015). By simulating IGM tomographic observations with realistic signal-to-noise, resolution, and sightline separation, we have shown that the reconstructed flux fields visually match the underlying dark matter density (Lee et al. 2014a) and can be used to find high-redshift protoclusters and voids (Stark et al. 2015b,a). Moreover, sufficiently large surveys (with $\gtrsim 1$ deg of contiguous sky coverage) can recover kinematically-defined cosmic web classifications with a fidelity comparable to low-redshift surveys using the galaxy density field (Lee & White 2016). These results suggest that IGM tomography could allow measurement of galaxy shape-cosmic web alignments at $z \sim 2.5$ in the near future.

In this paper, we will discuss the prospects for measuring galaxy-cosmic web alignments using IGM tomography surveys with mean sightline separations of $\langle d_{\perp} \rangle = [1.4, 2.5, 4, 6.5] h^{-1}$ Mpc. These reflect both existing and possible future surveys. Firstly, $\langle d_{\perp} \rangle = 2.5 h^{-1}$ Mpc reflects the ongoing COSMOS Lyman-Alpha Mapping And Tomography Observations (CLAMATO) survey (for which the pilot phase is being completed; see Lee et al. 2014b, 2016), which aims to cover ~ 1 deg² in the COSMOS field using the LRIS spectrograph on the 10.3-m Keck-I telescope. CLAMATO will cover a redshift range $2.2 < z < 2.5$, mapping $\sim 10^6 h^{-3}$ Mpc³ comoving volume with a spatial resolution of $2.5 h^{-1}$ Mpc. By ~ 2020 , the Subaru Prime-Focus Spectrograph (PFS) will begin operation (Takada et al. 2014), and an IGM tomographic survey building on the PFS galaxy evolution survey, but obtaining additional sightline spectra and higher S/N, could cover ~ 20 deg² with $\langle d_{\perp} \rangle = 4 h^{-1}$ Mpc. On the other hand, an IGM tomography map could be constructed “for free” using the $i < 24$ LBGs targeted for the PFS Galaxy Evolution Survey (Takada et al. 2014) without additional IGM tomography targets, yielding $\langle d_{\perp} \rangle = 6.5 h^{-1}$ Mpc. Finally, the proposed FOBOS instrument on Keck will offer much greater ($\sim 10\times$) multiplexing and field-of-view than LRIS on the same telescope, allowing for deeper integrations and hence denser sightline sampling of $\langle d_{\perp} \rangle \sim 1.4 h^{-1}$ Mpc while surveying ~ 1 deg², similar to CLAMATO.

In this paper, we will estimate the quality of cosmic web direction measurements (e.g. direction of filaments, normal vector to sheets, etc.) using mock observations based on the Nyx hydrodynamic IGM simulations. We will discuss the feasibility for measuring galaxy-cosmic web alignments using these surveys in tandem with coeval galaxy samples at $z \sim 2.5$.

2. METHODS

2.1. Nyx simulations and mock observations

We use a cosmological hydrodynamical simulation generated with the N-body plus Eulerian hydrodynamics NYX code (Almgren et al. 2013). It has a $100 h^{-1}$ Mpc box size with 4096^3 cells and particles, resulting in a dark matter particle mass of $1.02 \times 10^6 h^{-1} M_\odot$ and spatial resolution of $24 h^{-1}$ kpc. As discussed in Lukić et al. (2015), this resolution is sufficient to resolve the filtering scale below which the IGM is pressure supported and to reproduce the flux statistics at percent accuracy at redshift $z = 2.4$. The box covers a similar size to the proposed CLAMATO and FOBOS survey volumes. We use a flat Λ CDM cosmology with $\Omega_m = 0.3$, $\Omega_b = 0.047$, $h = 0.685$, $n_s = 0.965$, and $\sigma_8 = 0.8$, consistent with latest Planck measurements (Planck Collaboration et al. 2016).

In NYX, the baryons are modeled as an ideal gas on a uniform grid. The baryons have a primordial composition with hydrogen and helium mass abundances of 75% and 25%, respectively. We account for photoionization, recombination, and collisional excitation of all neutral and ionized species of hydrogen and helium, which evolve in ionization equilibrium with the uniform UV background given by Haardt & Madau (2012), with the mean flux normalized to match observational values. See Lukić et al. (2015) for the reaction and cooling rates used in the code. This simulation does not model star-formation and hence has no feedback from stars, galaxies, or AGNs, but these are expected to have a negligible effect on the Ly α forest statistics (Viel et al. 2013). Future Nyx IGM simulations will include galaxy formation physics in order to self-consistently simulate a galaxy population, allowing better interpretation of the relationship between galaxies and the Ly α forest.

We generated 512^2 absorption skewers with a spacing of $0.2 h^{-1}$ Mpc and sampled from these skewers to create mock data. We computed the Ly α forest flux fluctuation along each skewer

$$\delta_F = F/\langle F \rangle - 1 \quad (1)$$

where $F = \exp(-\tau)$ and τ is the Ly α optical depth, computed in redshift space and Doppler broadened using the gas temperature. Hereafter we refer to δ_F as the flux.

We then create mock spectra that reflect the data quality expected from current and upcoming surveys. First, we randomly select absorption skewers with the appropriate mean sightline spacing $\langle d_\perp \rangle$ and rebin them along the line of sight to a resolution of $0.78 h^{-1}$ Mpc, similar to the line-of-sight spectral resolution from the CLAMATO spectra.

We simulate noise by assuming the S/N per pixel is a unique constant for each skewer. To determine S/N for each skewer, we draw from a power-law S/N distribution

$dn_{\text{los}}/dS/N \propto S/N^{-\alpha}$ (Stark et al. 2015b; hereafter S15b), where S/N ranges between 1.5 (the minimum S/N in CLAMATO; Lee et al. 2014b, 2016) and infinity. Lee et al. (2014a) found that $\alpha \sim 2.5$ for the LBGs and QSOs that we target; however, as the sightline separation increases, the sources targeted become brighter and we move further along the exponential tail of the luminosity function, so α becomes larger. S15b find $\alpha = 2.9$ (3.6) for $\langle d_\perp \rangle = 2.5$ (4) h^{-1} Mpc, respectively. They did not determine α for sightline spacings $< 2 h^{-1}$ Mpc or $> 4 h^{-1}$ Mpc; therefore we use $\alpha = 2.7$ (3.6) for our $\langle d_\perp \rangle = 1.4$ (6.5) h^{-1} Mpc map by extrapolating the S15b values for $\langle d_\perp \rangle = 2$ (4) h^{-1} Mpc. We confirm the power-law distribution is appropriate by comparing it to the S/N distribution of observed pixels from the CLAMATO pilot observations. Using the simulated S/N distribution, we add noise to each pixel assuming a Gaussian distribution. We also model the effect of continuum-fitting error with an RMS of 10%: $F_{\text{obs}} = F_{\text{sim}}/(1 + \delta_{\text{cont}})$ where δ_{cont} is a random Gaussian deviate, identical for all pixels within a skewer, with mean 0 and standard deviation 0.1. This reflects the continuum-fitting uncertainties expected from data with comparable S/N (Lee et al. 2012).

For the tomographic reconstruction, we use the publicly available Wiener filter reconstruction code of Stark et al. (2015b)¹ to create a 3D map of the flux field. The Wiener filter is ideal for reconstruction as it provides a minimum variance estimate of the 3D field, assuming the field is normally distributed (Caucci et al. 2008, Lee et al. 2014a, Stark et al. 2015b). The reconstructed signal is

$$\hat{s} = \mathbf{S}_{\text{md}}(\mathbf{S}_{\text{dd}} + \mathbf{N})^{-1} \mathbf{d} \quad (2)$$

where \mathbf{d} is the data, \mathbf{N} is the noise covariance, \mathbf{S}_{md} is the map-data covariance, and \mathbf{S}_{dd} is the data-data covariance. We assume that the noise covariance is diagonal, so that $N_{ij} = n_i^2 \delta_{ij}$ where n_i is the simulated noise for each pixel. We further assume that $\mathbf{S}_{\text{md}} = \mathbf{S}_{\text{dd}} = S$:

$$S = \sigma_F^2 \exp \left[-\frac{\Delta x_\perp^2}{2l_\perp^2} - \frac{\Delta x_\parallel^2}{2l_\parallel^2} \right] \quad (3)$$

We use $\sigma_F^2 = 0.05$ and isotropic smoothing with $l_\parallel = l_\perp = \langle d_\perp \rangle$. Hereafter we refer to the reconstructed flux as δ_F^{rec} and the simulated flux as δ_F .

2.2. Defining the Cosmic Web

We measure the cosmic web directions using the eigenvectors of the deformation tensor, an approach inspired by the cosmic web classifications of Hahn et al. (2007b). While there are many alternative cosmic web classifiers (see enumeration in Cautun et al. 2014), we prefer the deformation tensor approach for a variety of reasons: it allows direct comparison with Lee & White (2016); it is physically motivated by the Zel'dovich approximation; and it is directly related to the gravitational shear field relevant for weak-lensing intrinsic alignments (Codis et al. 2015).

¹ <https://github.com/caseystark/dachshund>

The deformation tensor is defined as the Hessian of the gravitational potential Φ :

$$D_{ij} = \frac{\partial^2 \Phi}{\partial x_i \partial x_j} \quad (4)$$

The Hessian is most efficiently calculated in Fourier space, using the Poisson equation in suitable units where $4\pi G = 1$, $\nabla^2 \Phi = k^2 \Phi = \delta_k$. Therefore we can directly compute the Fourier transform of \tilde{D}_{ij} from the density:

$$\tilde{D}_{ij}(k) = \frac{k_i k_j}{k^2} \delta_k \quad (5)$$

and inverse-Fourier transform this quantity to obtain D_{ij} . To compute D_{ij} , we define δ as the sum of the matter and baryonic overdensity measured in redshift space, binned on a 128^3 grid and smoothed with a Gaussian kernel with standard deviation $R_G = 2 h^{-1}$ Mpc (see below for further description of smoothing). We then diagonalize the deformation tensor at every point in space to obtain its eigenvectors, \hat{e}_1 , \hat{e}_2 , and \hat{e}_3 (where the eigenvectors correspond to eigenvalues $\lambda_1 < \lambda_2 < \lambda_3$; in the Zel'dovich approximation, collapse proceeds first along \hat{e}_3 and last along \hat{e}_1). Note that the traceless tidal shear tensor

$$T_{ij} = \frac{\partial^2 \Phi}{\partial x_i \partial x_j} - \frac{1}{3} \nabla^2 \Phi \delta_{ij} \quad (6)$$

which is more relevant than D_{ij} for intrinsic alignment, shares its eigenvectors with the deformation tensor. As a result, we will use the phrases ‘‘eigenvectors of the tidal tensor’’ and ‘‘eigenvectors of the deformation tensor’’ interchangeably.

We define the cosmic web directions of the IGM tomography map, which reconstructs the Ly α forest flux, as the eigenvectors of the pseudo-deformation tensor (Lee & White 2016), where we simply substitute the Fourier transform of the flux field, δ_F , for δ_k in Equation 5. Since δ_F has the opposite sign as δ_k , we order the eigenvalues of the pseudo-deformation tensor from largest to smallest.

We classify each point as a node, filament, sheet or void using the number of eigenvalues greater than a nonzero threshold value λ_{th} , similar to Lee & White (2016) and Forero-Romero et al. (2009). A nonzero threshold leads to a better agreement with visually prominent sheets and filaments (Forero-Romero et al. 2009) and is justified because directions with a small positive λ are contracting so slowly they may not collapse in a Hubble time. Similar to Lee & White (2016), we choose $\lambda_{\text{th,m}}$ by matching the volumetric void fraction in the matter density to the $\sim 19\%$ void fraction of Stark et al. (2015a). We choose the threshold for the flux, $\lambda_{\text{th,F}}$, using the same condition on the void fraction for the $\langle d_{\perp} \rangle = 1.4, 2.5, 4, \text{ and } 6.5 h^{-1}$ Mpc reconstructions.

The eigenvectors of the deformation tensor are related to the underlying geometry and kinematics of the cosmic web. In the Zel'dovich approximation, matter is collapsing along the eigenvector when the eigenvalue is positive, and expanding along the eigenvector when the eigenvalue is negative (Hahn et al. 2007b). In a filament, there is only one negative eigenvalue, thus \hat{e}_1 is the only direction of expansion,

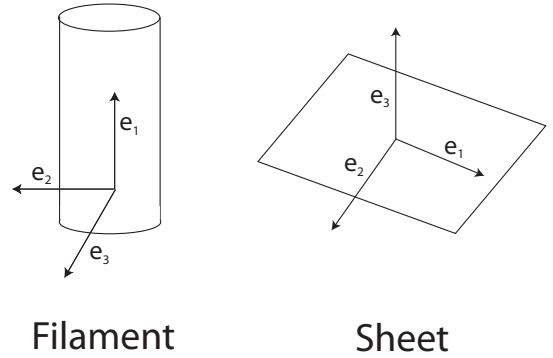


Figure 1. Relationship between eigenvectors of the tidal tensor (or equivalently, deformation tensor) and cosmic web directions.

making it the direction along which the filament is oriented. Similarly, in a sheet, there is only one positive eigenvalue, making \hat{e}_3 the normal vector to the sheet. Therefore, we define the directions of the cosmic web using the eigenvectors of the tidal tensor.

Following Lee & White (2016), we smooth the deformation tensor to minimize the effects of reconstruction noise and remove small-scale fluctuations. They found that a Gaussian kernel with $R_G \sim 1.5 \langle d_{\perp} \rangle$ was appropriate for this purpose (see also Caucci et al. 2008). Therefore, we use smoothing kernels with $R_G = [2, 4, 6, 10]$ for $\langle d_{\perp} \rangle = [1.4, 2, 4, 6.5]$ reconstructions. A larger smoothing scale leads to a more homogeneous map with less variation in δ_F^{rec} , so maps with a larger $\langle d_{\perp} \rangle$ have a smaller spread in δ_F^{rec} (Figure 2).

We also smooth the underlying matter density which we use for comparison. Since our cosmic web classification scheme is based on the Zel'dovich approximation, it is only valid up to the mildly nonlinear scales where the Zel'dovich approximation fails (Eardley et al. 2015). Therefore, smoothing on scales of a few h^{-1} Mpc is appropriate to eliminate highly non-linear scales. We choose a matter smoothing scale of $2 h^{-1}$ Mpc, comparable to the smoothing scales used in shape-cosmic web and spin-cosmic web alignment studies from simulations (see compilation in Forero-Romero et al. 2014).

The choice of smoothing scale is ultimately arbitrary; for instance, we could follow Lee & White (2016) and choose a different matter density smoothing scale for each reconstruction, matching the smoothing scales of the flux map and the matter. However, we prefer to use a single ‘‘true’’ matter map to generate galaxy spins (see Section 2.4). The results are qualitatively similar if we instead match the matter smoothing scale to the reconstruction smoothing scale, in that the recovery of the eigenvectors declines from $\langle d_{\perp} \rangle = 1.4 h^{-1}$ Mpc to $6.5 h^{-1}$ Mpc. However, the decline is much less steep if we match smoothing scales; thus, much of the misalignment between the matter field and IGM tomography maps with $\langle d_{\perp} \rangle > 2 h^{-1}$ Mpc is due to the mismatch in smoothing scales.

Figure 2 compares the matter density field to the reconstructed flux field for $\langle d_{\perp} \rangle = 1.4, 2.5, 4, \text{ and } 6.5 h^{-1}$ Mpc

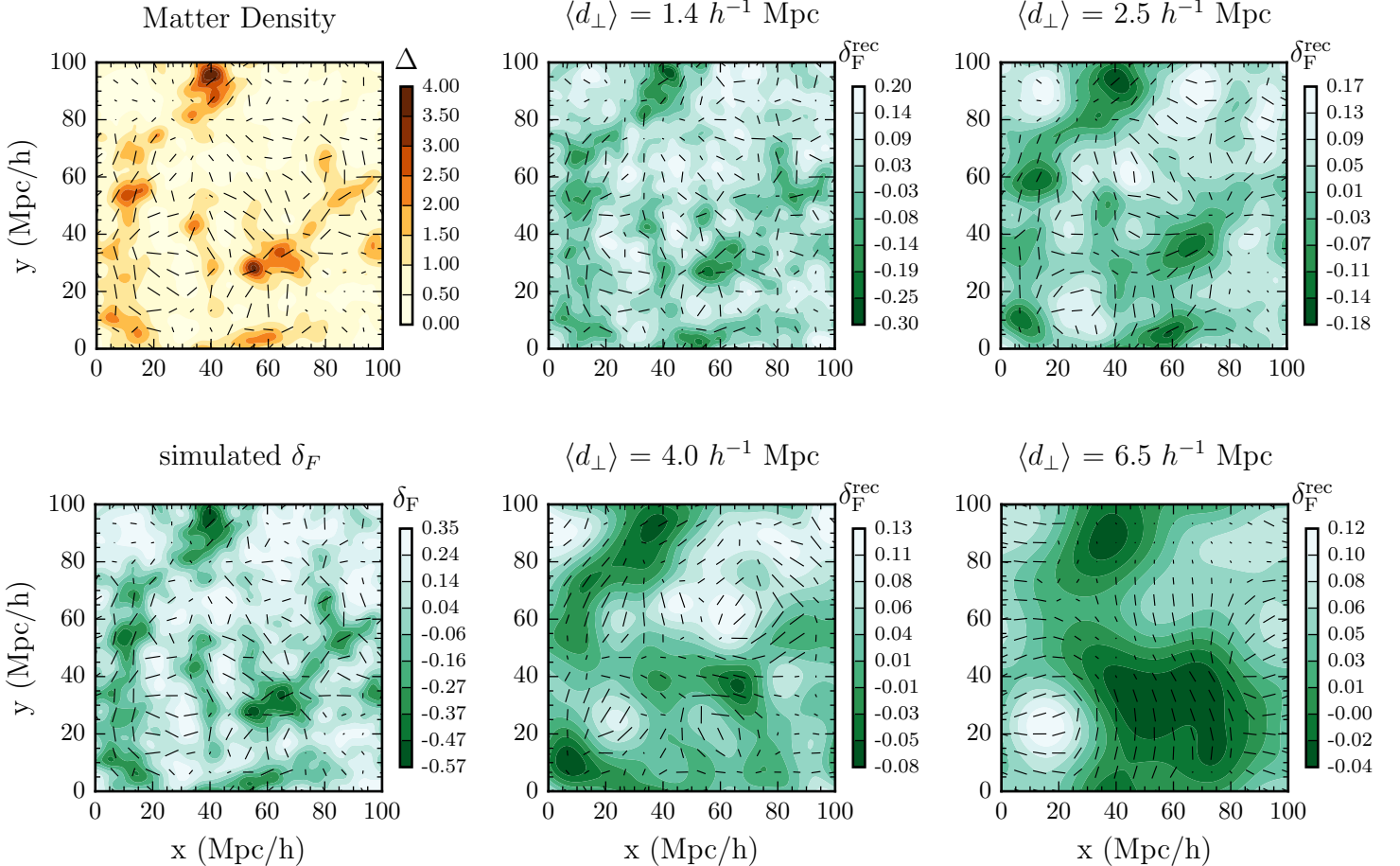


Figure 2. Matter density (dark matter plus baryons) and δ_F from the simulations (left) and δ_F^{rec} from simulated IGM tomography observations with varying $\langle d_{\perp} \rangle$ (right). All quantities are evaluated in redshift space. The figures show a slice through the full simulation box with width $0.8 h^{-1} \text{ Mpc}$ along the line of sight. The overplotted vectors are \hat{e}_1 determined from the corresponding field.

for an $0.8 h^{-1} \text{ Mpc}$ slice through the simulation box. We also show the simulated redshift-space δ_F field, equivalent to a “perfect resolution” IGM tomography survey. We publicly release the matter field, simulated δ_F , IGM tomography maps, and halo catalogs². We overplot headless vectors corresponding to the projection of \hat{e}_1 onto the xy plane; arrowheads are not displayed because the sign of \hat{e}_1 is arbitrary. The IGM tomography surveys are smoothed using the smoothing scales defined above, while the matter density and simulated flux field, δ_F , are smoothed with $R_G = 2 h^{-1} \text{ Mpc}$. The simulated flux and $\langle d_{\perp} \rangle = 1.4 h^{-1} \text{ Mpc}$ fields reproduce the matter density well, although with a very different dynamical range owing to the nonlinear transformation from δ to δ_F . The simulated flux and $\langle d_{\perp} \rangle = 1.4 h^{-1} \text{ Mpc}$ maps reproduce the small-scale structure in the matter-density \hat{e}_1 quite well, while larger smoothing scales yield a smoother distribution of δ_F^{rec} and \hat{e}_1 that captures the large-scale features but misses much of the smaller-scale structure.

² <http://tinyurl.com/hg7u4dg>

2.3. Galaxy spin observations

Measuring galaxy-cosmic web alignments at $z \sim 2.5$ requires a large galaxy sample with accurate redshifts and structural parameters. The typical half-light radius of a $z \sim 2.4$ galaxy is $\sim 0.3''$ (Giavalisco et al. 1996, Van Der Wel et al. 2014). Space-based or adaptive-optics observations are therefore preferred for measuring structural parameters at $z \sim 2.4$, although the shapes of faint galaxies can be measured well from the ground with deep exposures and $\sim 0.5''$ seeing (Chang et al. 2013). Additionally, LSST plans to measure cosmic shear out to $z \sim 3$ using ground-based observations with $0.7''$ mean seeing (LSST Science Collaboration et al. 2009).

Galaxy spins can be determined from galaxy images using the galaxy’s position angle and axis ratio assuming the galaxy is an oblate spheroid (Haynes & Giovanelli 1984). The position angle defines the direction of the projected major axis, while the inclination is calculated from the axis ratio, assuming the galaxy is circular if viewed face-on and the intrinsic thickness is known. As a result, this method is only applicable to spiral or spheroidal galaxies, which can be approximated as oblate spheroids (e.g Lee & Erdogdu 2007, Tempel

et al. 2013). For elliptical galaxies, alignments between the galaxy’s major axis and the projected eigenvectors of the tidal tensor are most relevant.

The spin axis is then assumed to be the minor axis of the galaxy ellipsoid. In principle the spin and minor axis may be misaligned, though both observations and simulations find small misalignments (Franx et al. 1991, Codis et al. 2015), $\sim 15^\circ$ at $z \sim 2$ (Wisnioski et al. 2015). High resolution or adaptive-optics IFU observations can measure the kinematic major axes of galaxies at $z \sim 2$ (e.g. Wisnioski et al. 2015), but even large surveys with KMOS or NIRSpec (Giardino et al. 2016) may only accumulate 1000 galaxies over the next several years, far smaller than the sample sizes expected from wide-field imaging surveys.

Galaxies at $z \sim 2$ have a clumpier and more irregular morphology than galaxies at low redshift (Lotz et al. 2006). This may present an additional challenge for measuring the major axis and ellipticity of the light profile. In addition, the intrinsic thickness is a major source of systematic error in determining the inclination: it varies by morphology (Haynes & Giovanelli 1984) and potentially also with redshift, as galaxies at $z \sim 2$ are thicker than galaxies at low redshift (Law et al. 2012). Furthermore, only the absolute value of the inclination is measurable, so there will always be a degeneracy between spins pointing towards the observer and spins pointing away from the observer, except for face-on or edge-on galaxies. Alignment studies have attempted to mitigate this degeneracy in several ways (Lee & Erdogdu 2007, Varela et al. 2012, Slosar & White 2009, Pahwa et al. 2016, Trujillo et al. 2006) but ultimately the degeneracy will degrade the measured alignment signal.

To understand the impact of these systematics on alignment measurements at $z \sim 2$, we include realistic errors in the galaxies’ position angles and inclinations. Since the inclination measurements may be particularly impacted by systematic errors from the unknown intrinsic thickness and anisotropies in the PSF, we consider both 3D and 2D alignment measurements, where the 2D alignment measurements ignore the z -direction of the eigenvectors altogether. To model the spin degeneracy, we randomly select each spin to face either towards or away from the observer.

2.4. Galaxy alignment model

We wish to remain agnostic about the mechanisms and strength of the galaxy-cosmic web alignment signal. Hence, we assign galaxy spins to the simulation halos using a stochastic relationship between the eigenvectors of the tidal tensor of the matter density field and galaxy spin. This prescription allows us greater flexibility to adjust the strengths of galaxy alignments compared to adhering to the results of a single simulation. The galaxy formation physics governing the shape-cosmic web relationship at $z \sim 2$ are not well understood, so flexibility in modeling this relationship is valuable. Moreover, it is not clear which eigenvector the spin is most strongly aligned with, so our model allows us to adjust the alignment strength with any of the three eigenvectors.

Our model takes as input $\langle \cos \theta \rangle$, the mean of the cosine of the angle between the galaxy spins and the local eigenvector

of the matter field tidal tensor. We parametrize the PDF of $\mu \equiv \cos \theta$ as

$$P(\mu) = a\mu^2 + c \quad (7)$$

where $c = 1 - a/3$ such that $P(\mu)$ is normalized. For simplicity, we consider only the alignment with a single eigenvector at a time.

To compare to various observational and simulation results, we parameterize $P(\mu)$ using $\langle \cos \theta \rangle$ rather than a :

$$a = 12\langle \cos \theta \rangle - 6 \quad (8)$$

Equation 7 roughly reproduces $P(\mu)$ as measured from simulations. A representative value of $\langle \cos \theta \rangle$ is given by the simulations of Codis et al. (2015), $\langle \cos \theta \rangle = 0.509$. This value is similar to $\langle \cos \theta \rangle$ for \hat{e}_1 -spin alignments measured at low redshift (Tempel & Libeskind 2013, Zhang et al. 2013, Pahwa et al. 2016) and spin-filament alignments in simulations (Dubois et al. 2014) and observations (Tempel et al. 2013). Moreover, for small deviations from random alignments, Equation 7 agrees well with Equation 5 in Lee & Erdogdu (2007), who derive an analytic expression for the misalignment angle between galaxy spin and \hat{e}_2 in tidal torque theory.

To assign each galaxy a spin axis, we start by assigning a redshift-space error drawn from a normal distribution with standard deviation σ_v (see Section 2.5). Next, we find the eigenvectors of the tidal tensor of the matter density field at the nearest grid point to the galaxy’s redshift-space position, including redshift error. The misalignment angle θ is randomly drawn from Equation 7 and the azimuthal angle ϕ from the uniform distribution between 0 and 2π . Since both the eigenvectors and the galaxy spin axis are headless vectors, we randomly generate a direction for the galaxy spin as well. Last, we add a random Gaussian deviate with standard deviation σ_{PA} (σ_i) to the position angle (inclination), and randomly choose whether the galaxy spin will be oriented towards or away from the observer.

2.5. IGM and galaxy survey parameters

Our fiducial parameters are sightline spacing of $2.5 h^{-1}$ Mpc, coeval sample of 10000 galaxies, redshift errors of 100 km s^{-1} , $\sigma_{\text{PA}} = 10^\circ$ and $\sigma_i = 10^\circ$.

We consider how the measurable significance of the alignment signal varies with different sightline spacings, galaxy sample sizes and assumed errors. We use sightline spacings of 6.5, 4.0, 2.5, and $1.4 h^{-1}$ Mpc, as well reconstructions of the full noiseless δ_F simulation grid (with $0.8 h^{-1}$ Mpc voxels) as the limiting case of “perfect” IGM tomography. The 4.0, 2.5, and $1.4 h^{-1}$ Mpc spacings correspond to the sightline spacings expected for the PFS, CLAMATO, and FOBOS IGM tomography surveys, respectively, while $6.5 h^{-1}$ Mpc is the sightline spacing of an IGM reconstructions using only the baseline PFS galaxy evolution survey (Takada et al. 2014) without incorporating additional targets for tomography.

We use coeval galaxy samples of 600, 3000, 10000 and 30000 galaxies. The density of target galaxies for tomography differs by an order of magnitude between the $\langle d_\perp \rangle = 1.4$ and $4.0 h^{-1}$ Mpc cases, so the galaxy samples were chosen to span an order of magnitude as well, allowing us to directly

compare the importance of coeval galaxy sample size versus sightline density. The fiducial 10000 galaxy sample does not require 10000 galaxies in 1 deg^2 (the angular size of our simulation box at $z \sim 2.4$); rather, the galaxies may be spread over a wider area if the tomographic map also has the same coverage. The cosmic web recovery does not depend on halo mass of the galaxies (Figure 5), so we emulate a survey with larger area by simply including lower-mass galaxies in our sample.

The 10000 galaxy sample is similar to the number of $2.15 < z < 2.55$ redshifts that the PFS galaxy evolution survey could obtain. Structural parameters for such a sample could be measured either from the deep HyperSuprimeCam imaging used for PFS targeting or from wide-field space-based imaging from Euclid or WFIRST. More ambitious upcoming surveys could obtain even larger samples of coeval galaxies, such as the proposed ‘‘Billion-Object Apparatus’’, which could measure redshifts for 10^5 coeval galaxies per square degree in the 2030s (Dodelson et al. 2016) — as a conservative choice, we therefore include a 30000 galaxy sample to represent these futuristic surveys. At the other extreme, we also consider a 600 galaxy sample, roughly matching the number of coeval galaxies in the CLAMATO volume, primarily from the zCOSMOS-deep survey (Scoville et al. 2007, Lilly et al. 2007).

The fiducial redshift errors are 100 km s^{-1} , appropriate for redshifts from nebular emission lines in restframe optical spectra (Steidel et al. 2010). We consider redshift errors of 300 km s^{-1} , appropriate for redshifts from UV absorption lines or $\text{Ly}\alpha$ emission lines (Steidel et al. 2010, Kriek et al. 2015), and 500 km s^{-1} , appropriate for emission-line redshifts from grism spectra (Kriek et al. 2015, Momcheva et al. 2016). We also consider the maximal redshift errors allowed by our box size, in which the z position of each galaxy in the box is drawn from a uniform distribution. This produces a distribution with $\sigma_v \sim 2000 \text{ km s}^{-1}$, somewhat better than typical photometric redshifts ($\sigma_v \gtrsim 9000 \text{ km s}^{-1}$) or $\text{Ly}\alpha$ tomographic redshifts ($\sigma_v \gtrsim 3000 \text{ km s}^{-1}$; Schmittfull & White 2016).

The fiducial error on the galaxy position angle is 10° , consistent with position angle errors as estimated from both cosmic shear measurements from HST imaging (Leauthaud et al. 2007, Joachimi et al. 2013) and from structural parameter measurements using CANDELS imaging (Van Der Wel et al. 2012)³ for galaxies with magnitudes, sizes, and Sersic indices typical of $z \sim 2$ galaxies. We also consider position angle errors of 5° and 20° in order to determine the importance of imaging quality. These position angle errors may not be appropriate for ground-based imaging, which generally suffers from increased uncertainty in shape modeling (e.g. Chang et al. 2013). We therefore also consider position angle errors of 40° , which may be more realistic for structural

parameters derived from ground-based imaging.

We use a fiducial inclination error of 10° . The error on the inclination can be related to the error on the ellipticity using Taylor series error propagation. Using the ellipticity errors from the CANDELS catalog for $z \sim 2$ galaxies assuming intrinsic thickness 0.25 (Van Der Wel et al. 2012), we find a median $\sigma_i = 6^\circ$. To conservatively account for systematic errors from the intrinsic thickness, the fiducial value of σ_i is 10° . We also consider $\sigma_i = 5^\circ$ and $\sigma_i = 20^\circ$ to determine the impact of inclination error on our measurement.

For each measurement, we simulate galaxy selection by randomly selecting N_{gal} halos with $M_h > 10^{10.5} M_\odot$. While this does not reflect a realistic selection function, the cosmic web recovery does not depend on mass (Figure 5) so we expect similar results for realistic selection functions. This also allows us to mock up larger-area surveys without using a larger simulation box, as we can simply select more galaxies within the same $100 h^{-1} \text{ Mpc}$ volume.

To simulate the cosmic web-galaxy spin alignment measurement, we measure $\langle \cos \theta_{rg} \rangle$, the dot product of the reconstructed eigenvector and the galaxy spin, as a function of $\langle \cos \theta_{eg} \rangle$, where θ_{eg} is the angle between the matter field eigenvector and the galaxy spin. We turn this into a significance above random by subtracting 0.5, the mean of $\cos \theta$ for a random distribution, and dividing by the standard deviation of 1000 simulations of the measurement. For 2D measurements, the significance is defined as $\langle \theta_{rg} \rangle - \pi/4$ divided by the standard deviation, since a random vector in 2D follows a uniform distribution in θ .

3. RESULTS

3.1. Recovery of cosmic web directions

We first compare our cosmic web classification to Lee & White (2016), who use an N-body simulation rather than a hydrodynamic IGM simulation and match the DM and IGM tomography smoothing scales. We confirm their finding that IGM tomography can recover cosmic web classifications with similar fidelity to low-redshift surveys, suggesting this finding is insensitive to the details of the simulation and the choice of smoothing scale.

The fraction of the volume with $\Delta N^+ = 0$ is somewhat lower in our $\langle d_\perp \rangle = 2.5 h^{-1} \text{ Mpc}$ reconstruction than that of Lee & White (2016), as they find [15,69,15]% of the volume was classified within [-1,0,+1] eigenvalues. However, we do not match the matter smoothing scale to the IGM tomography smoothing scale and we include continuum errors in our mock absorption skewers, both of which degrade the reconstructions. Compared to Lee & White (2016), we recover sheets, voids, and filaments with slightly lower fidelity, and nodes with significantly lower fidelity.

³ These methods differ most importantly in that the weak-lensing analyses are somewhat more careful about accounting for systematic errors from PSF variation than the galaxy shape analyses. Also, the weak-lensing anal-

yses present their results in terms of error on the galaxy polarization or ellipticity, while the galaxy shape analyses directly report the errors on the position angle. Polarization/ellipticity errors can be translated to PA errors using Taylor series error propagation.

Table 1. Fidelity of Cosmic Web Classification

$\langle d_{\perp} \rangle$ (h^{-1} Mpc)	Smoothing (h^{-1} Mpc)	Flux Eigenvalue Threshold	Fraction by ΔN^+ (%)				Volume overlap (%)		
			-1	0	1	Node	Filament	Sheet	Void
δ_F	2	$\lambda_{\text{th},F} < -0.0175$	8.8	83.9	7.2	67.0	82.9	85.2	84.7
1.4	2	$\lambda_{\text{th},F} < -0.0101$	15.2	69.2	14.7	45.7	66.1	72.8	67.5
2.5	4	$\lambda_{\text{th},F} < -0.0095$	17.9	61.1	18.9	24.0	54.2	67.3	60.2
4.0	6	$\lambda_{\text{th},F} < -0.0090$	22.4	52.5	20.7	16.7	46.8	59.3	48.3

NOTE— $\Delta N^+ = N_{\text{matter}}^+ - N_F^+$ where N^+ is the number of eigenvalues with $\lambda > \lambda_{\text{th}}$ in a given map. Fraction by ΔN^+ refers to the volume fraction of the map where ΔN^+ has that value. Volume overlap is the fraction of all points classified as a particular web element in the matter field that are also classified as that web element in the flux map. We use $\lambda_{\text{th},m} = 0.043$ and a smoothing scale of $2 h^{-1}$ Mpc for the matter field.

Figure 3 displays the PDF of $\cos \theta$, where θ is the misalignment angle between the matter field tidal tensor eigenvectors and the pseudo-deformation tensor eigenvectors from the reconstructed IGM maps. We also compute the misalignment angle PDF between the matter field tidal tensor eigenvectors and the pseudo-deformation tensor eigenvectors from the simulated δ_F smoothed on $2 h^{-1}$ Mpc scales, equivalent to an idealized reconstruction with no instrumental noise and infinite sightline density.

The mock surveys with $\langle d_{\perp} \rangle < 5 h^{-1}$ Mpc recover the eigenvectors of the tidal tensor at high significance. The recovery of the eigenvectors degrades quickly for $\langle d_{\perp} \rangle > 5 h^{-1}$ Mpc, due in part to the mismatch between $\langle d_{\perp} \rangle$ and the $2 h^{-1}$ Mpc smoothing scale of the matter field. The mean of the cosine of the misalignment angle for $[\hat{e}_1, \hat{e}_2, \hat{e}_3]$ is [0.874, 0.809, 0.901] for $\langle d_{\perp} \rangle = 1.4 h^{-1}$ Mpc, [0.813, 0.716, 0.833] for $\langle d_{\perp} \rangle = 2.5 h^{-1}$ Mpc, [0.736, 0.629, 0.757] for $\langle d_{\perp} \rangle = 4.0 h^{-1}$ Mpc, and [0.573, 0.508, 0.600] for $\langle d_{\perp} \rangle = 6.5 h^{-1}$ Mpc. Errors on these quantities are $< 0.1\%$. The mean of the cosine of the misalignment angle between is [0.945, 0.921, 0.967] using the simulated δ_F field. This is the upper limit of how well Ly α absorption measurements can measure the eigenvectors of the tidal tensor.

We also compute the mean of the misalignment angle at halo positions only. For $[\hat{e}_1, \hat{e}_2, \hat{e}_3]$, we find means of [0.891, 0.837, 0.919] for $\langle d_{\perp} \rangle = 1.4 h^{-1}$ Mpc, [0.815, 0.722, 0.838] for $\langle d_{\perp} \rangle = 2.5 h^{-1}$ Mpc, [0.734, 0.628, 0.761] for $\langle d_{\perp} \rangle = 4.0 h^{-1}$ Mpc, [0.571, 0.516, 0.607] for $\langle d_{\perp} \rangle = 6.5 h^{-1}$ Mpc, and [0.950, 0.929, 0.970] for simulated δ_F . The differences between these values and the means of $\cos \theta$ using the entire grid are quite modest, although statistically significant.

Figure 4 shows the quality of cosmic web recovery as a function of cosmic web type as classified in the matter map, using the $\langle d_{\perp} \rangle = 2.5 h^{-1}$ Mpc reconstruction. Mirroring the results in Table 1, \hat{e}_1 , \hat{e}_2 , and \hat{e}_3 are recovered worst in nodes. Despite the relatively high volume overlap for the void recovery, the tidal tensor eigenvectors are recovered slightly worse in voids than in anisotropic structures such as filaments and sheets. All three eigenvalues are similar in voids,

possibly causing confusion between perpendicular eigenvalues and leading to the poorer recovery of the cosmic web in voids. The recovery of eigenvectors in sheets and filaments are similar, although \hat{e}_1 is recovered better in filaments while \hat{e}_3 is recovered better in sheets. This is unsurprising given the connection between the eigenvectors and the geometry of the cosmic web, as \hat{e}_1 in filaments and \hat{e}_3 in sheets correspond to inherently anisotropic directions that should be easier to recover.

We additionally test the quality of the reconstruction as a function of halo mass. We divide the halo catalog into four bins and measure the angle between the eigenvectors in the matter field and the eigenvectors in the $\langle d_{\perp} \rangle = 2.5 h^{-1}$ Mpc reconstruction using the nearest grid point in redshift space. The recovery of the eigenvectors is nearly independent of the halo mass (Figure 5). None of the distributions are significantly different at the $p = 0.05$ level (2 sigma) according to Kolmogorov-Smirnov tests, implying that the eigenvectors can be recovered accurately at galaxy positions independent of halo mass.

We provide the first assessment of the accuracy of tidal tensor reconstruction by comparing the tidal tensor eigenvectors from the matter field to the tidal tensor eigenvectors from realistic mock observations. We expect that IGM tomography will be better at recovering the tidal tensor eigenvectors than using the galaxy positions from existing or upcoming galaxy surveys at the same redshift, such as zCOSMOS or PFS; these will provide much coarser cosmic web maps with galaxy separations of 9 (13) h^{-1} Mpc for PFS (zCOSMOS) (Diener et al. 2013, Takada et al. 2014). For instance, since protocluster identification with zCOSMOS required additional follow-up spectroscopy (Diener et al. 2015), the zCOSMOS redshift survey alone may be insufficient to measure the cosmic web at $z > 2$. In addition, cosmic web maps from IGM tomography are free from many of the biases that make measuring the cosmic web from spectroscopic $z \sim 2$ galaxy surveys difficult: these surveys have complex selection functions (e.g. Diener et al. 2013), inaccurate and/or biased redshift estimates (e.g., Adelberger et al. 2005, Steidel

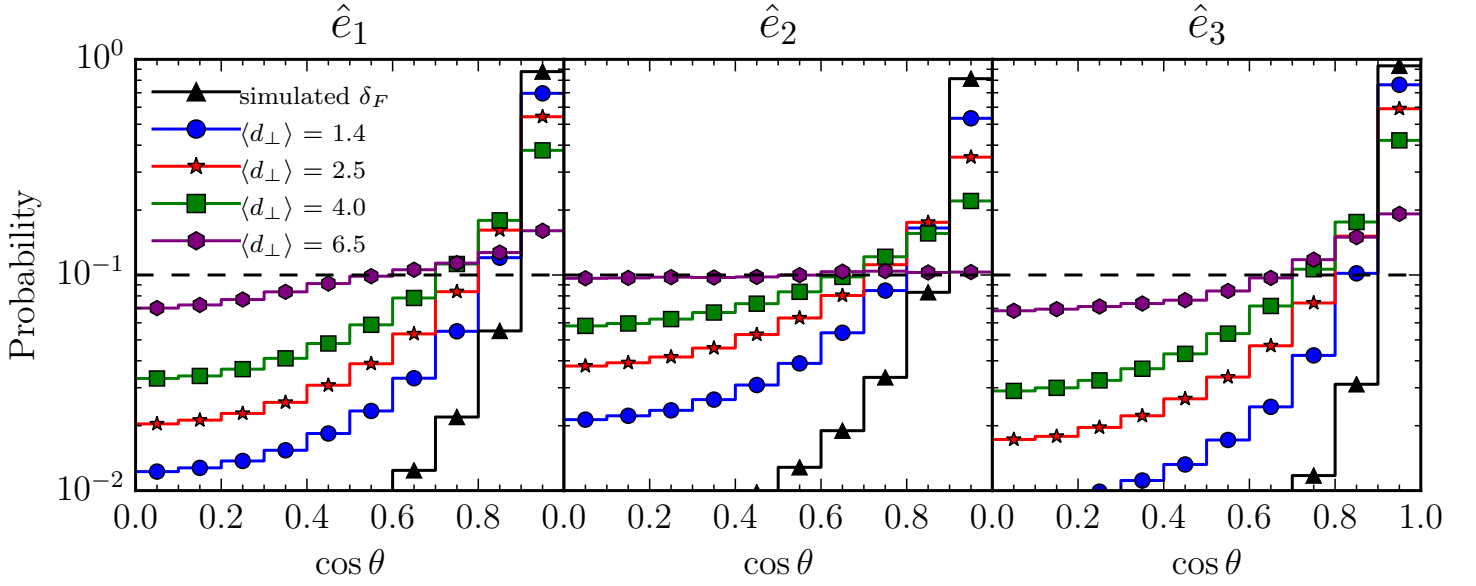


Figure 3. PDF of the cosine of the misalignment angle between the cosmic web directions from the matter density field and the cosmic web directions from the simulated IGM tomography observations. We also show the misalignment angle between the matter density cosmic web and the cosmic web computed from the simulated δ_F with $2 h^{-1}$ Mpc smoothing, which is the ideal case of a perfect reconstruction from Ly α forest data. In all cases the matter density field is smoothed on $2 h^{-1}$ Mpc scales. The horizontal dashed line is the distribution expected for random alignments.

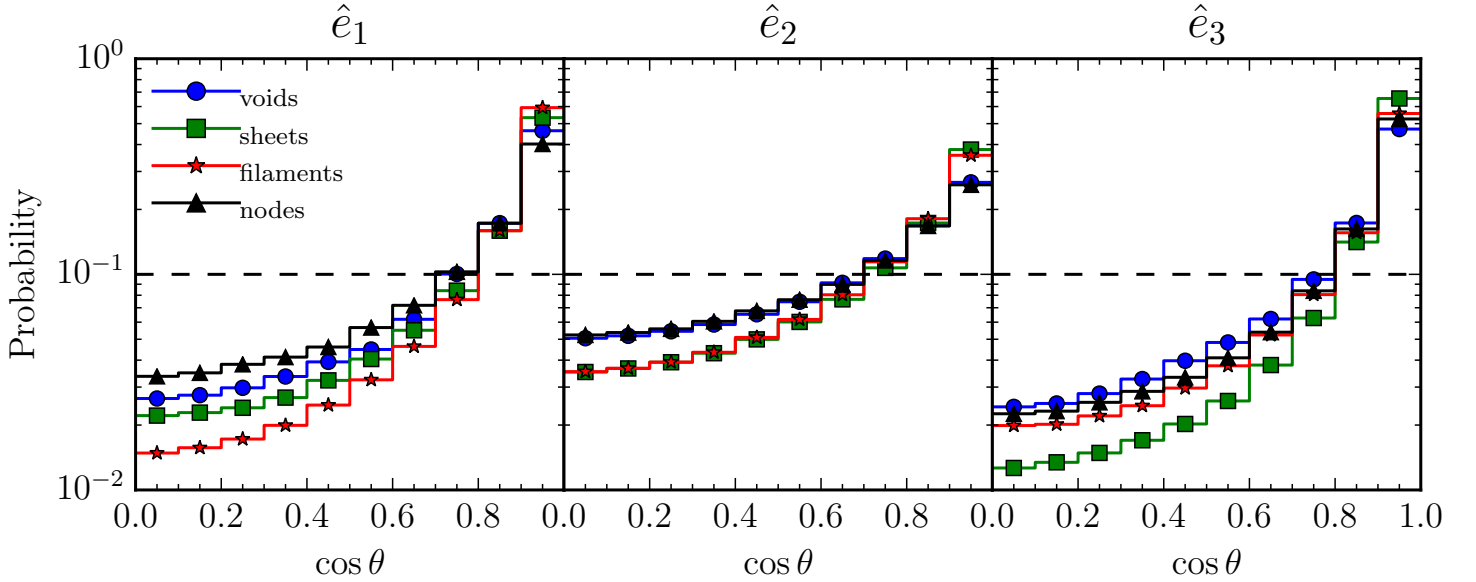


Figure 4. PDF of the cosine of the misalignment angle between the cosmic web directions from the matter density field and the cosmic web directions from the simulated IGM tomography observations, using the $\langle d_\perp \rangle = 2.5 h^{-1}$ Mpc reconstruction and splitting by classification from the matter map. All distributions are significantly different according to Kolmogorov-Smirnov tests.

et al. 2010, Rakic et al. 2012), cannot detect close pairs due to slit collisions (Wilson et al. 2015), and preferentially select star forming galaxies, which may be biased towards particular regions of the cosmic web (Alpaslan et al. 2015). In contrast, IGM tomography sightlines provide an unbiased sampling of the foreground cosmic web, and errors from pixel noise and continuum errors are well-understood, making a subdominant contribution to errors in the reconstruction.

3.2. Predictions for galaxy-cosmic web alignment measurements

Several workers have considered the alignment of galaxies and the cosmic web in simulations, but thus far observational studies of the galaxy-cosmic web alignment have generally been restricted to low redshift ($z \lesssim 0.5$) where sufficiently large galaxy catalogs exist to measure the cosmic web (Lee & Pen 2002, Lee & Erdogdu 2007, Tempel et al. 2013, Tempel & Libeskind 2013, Zhang et al. 2013, 2015, Pahwa et al. 2016; although see Malavasi et al. 2016 for recent results at $\langle z \rangle \sim 0.7$). We now consider the prospects for a galaxy-cosmic web alignment study at $z \sim 2$ using the cosmic web from IGM tomography maps and coeval galaxy samples from space-based or large ground-based telescopes.

First, we estimate the significance of the measured galaxy-eigenvector alignment signal as a function of the true strength of the galaxy-eigenvector alignment. We describe the PDF of the true galaxy-eigenvector misalignment angle using Equa-

tion 7, and thus parameterize the galaxy-eigenvector alignment strength using the deviation of $\langle \cos \theta \rangle$ from 0.5 (i.e. the deviation from random alignments):

$$\Delta \langle \cos \theta \rangle \equiv \langle \cos \theta \rangle - 0.5 \quad (9)$$

The significances computed from the measured $\langle \cos \theta \rangle$ are similar to other reasonable choices for estimators, such as using the difference between the number of aligned and anti-aligned galaxies. Note that the significance of a model with $-\Delta \langle \cos \theta \rangle$ is identical to the significance of a model with $\Delta \langle \cos \theta \rangle$ because the spins and eigendirections are headless vectors invariant under the transformation $\theta \rightarrow \pi - \theta$. Therefore, we only plot significances as a function of positive $\Delta \langle \cos \theta \rangle$.

In Figure 6, we show the forecasted significance of the alignment signal between galaxies and \hat{e}_1 , as a function of the sightline spacing, number of galaxies, expected redshift error, and errors on the galaxy position angle and inclination. Our fiducial values for these quantities are $\langle d_{\perp} \rangle = 2.5 h^{-1} \text{ Mpc}$, 10000 coeval galaxies, redshift errors of 100 km s^{-1} , and position angle and inclination errors of 10° . The $1-\sigma$ error on $\Delta \langle \cos \theta \rangle$ of ~ 0.01 for the fiducial measurement of alignment with \hat{e}_1 is somewhat larger than $1-\sigma$ errors from alignment measurements using low-redshift galaxies (~ 0.005 for similar galaxy sample sizes in Tempel et al. 2013, Tempel & Libeskind 2013, Pahwa et al. 2016).

Table 2. Summary of alignment models

$\Delta \langle \cos \theta \rangle$	Description	Reference
0.009	$z \sim 1.2$ alignments between \hat{e}_1 and galaxy spin from HorizonAGN	Codis et al. (2015)
0.020	$z \sim 2.3$ alignments between filaments and galaxy spins from HorizonAGN	Dubois et al. (2014)
0.054	$z \sim 1.05$ alignment between \hat{e}_1 and halo shape (N-body), plus misalignment between halo shape and galaxy shape, alignments extrapolated to $z \sim 2.4$ and $M_h \sim 10^{12} M_{\odot}$ assuming alignments constant as a function of M_h	Hahn et al. (2007a), Okumura et al. (2009)
0.092	$z \sim 1.05$ alignment between \hat{e}_1 and halo shape (N-body), plus misalignment between halo shape and galaxy shape, alignments extrapolated to $z \sim 2.4$ and $M_h \sim 10^{12} M_{\odot}$ assuming alignments constant as a function of M_h/M_{nt}	Hahn et al. (2007a), Okumura et al. (2009)

NOTE—Alignment models considered in Figure 6. See text for details. Each alignment model is parameterized using Equation 7 with $\langle \cos \theta \rangle = 0.5 + \Delta \cos \theta$.

Figure 6 shows the significance of alignment measurements between galaxy spins and \hat{e}_1 , \hat{e}_2 , and \hat{e}_3 as a function of the true alignment strength between galaxy spin and \hat{e}_1 , \hat{e}_2 and \hat{e}_3 . Consistent with Figure 3, alignments with \hat{e}_1 and \hat{e}_3 can be detected at similar levels of significance, while alignments with \hat{e}_2 will be detected with somewhat lower signif-

icance. We note that \hat{e}_2 alignments are detected at similar significance for both 2D and 3D measurements. We attribute this to redshift-space distortions in the map, which cause \hat{e}_2 to lie preferentially in the plane of the sky, because the directions of maximal and minimal compression (\hat{e}_1 and \hat{e}_3) are biased towards the line of sight due to compression and

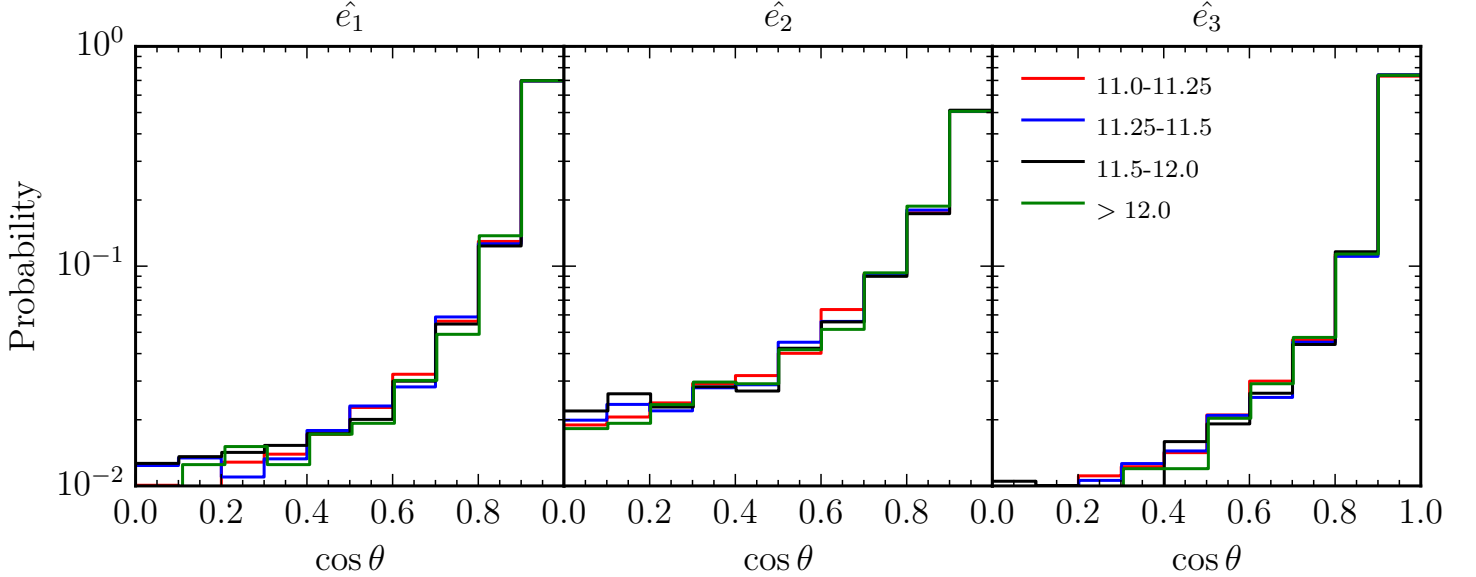


Figure 5. PDF of the cosine of the misalignment angle between the cosmic web directions from the matter density field and the cosmic web directions from the simulated IGM tomography observations, using the $\langle d_{\perp} \rangle = 2.5 h^{-1} \text{ Mpc}$ reconstruction. Misalignment angles are computed at the nearest grid point for each dark matter halo. The four groups are labeled by halo mass in units of $\log M_{\odot}$.

rarefaction from redshift-space distortions. Measuring alignments between \hat{e}_2 from the real-space density field and \hat{e}_2 from skewers generated using the real-space τ yields a similar reduction in the 2D \hat{e}_2 alignment signal as for the 2D \hat{e}_1 and \hat{e}_3 alignment signals.

Tidal torque theory predicts that galaxy spin is aligned with \hat{e}_2 . Using an analytic quadratic alignment model (Lee & Pen 2000), Lee & Erdogdu (2007) derive a PDF for the misalignment angle as a function of c , a correlation parameter ranging from 0 (random alignments) to 1 (perfect spin-shear alignments). In the limit of small $\Delta \langle \cos \theta \rangle$, this PDF can be well approximated by Equation 7. For our fiducial \hat{e}_2 alignment measurement we find a $1\text{-}\sigma$ error on $\Delta \langle \cos \theta \rangle \sim 0.015$, which translates to a $1\text{-}\sigma$ error on $c \sim 0.08$. Previous measurements at low redshift have achieved lower error bars: Lee & Pen (2002) find $c = 0.28 \pm 0.07$ ⁴, Lee & Erdogdu (2007) find $c = 0.08 \pm 0.01$, and Lee & Pen (2007) find $c = 0.0 \pm 0.05$ for red galaxies and $c = 0.33 \pm 0.07$ for blue galaxies. If $c \sim 0.2 - 0.3$ at $z \sim 2.4$, IGM tomography surveys with $\langle d_{\perp} \rangle = 2.5 h^{-1} \text{ Mpc}$ and 10000 coeval galaxies will measure this alignment at $\sim 3\sigma$. However, nonlinear evolution is expected to decrease the alignment between spin and \hat{e}_2 over time (Porciani et al. 2002), leading to a larger value of c at high redshift than low redshift. Regardless, these results suggest that the combination of galaxy surveys at low redshift and IGM tomography surveys at high redshift may be able to constrain the redshift evolution of the alignment and thus provide a more rigorous test of tidal torque theory than current studies.

⁴ Lee & Pen (2002) expresses their result in terms of $a_T = (3/5)c$. See Lee & Pen (2001) for the difference between a_T and c .

Figure 6 shows the importance of varying different parameters of the IGM and galaxy observations. Varying the sightline spacing from $\langle d_{\perp} \rangle = 1.4 h^{-1} \text{ Mpc}$ to $\langle d_{\perp} \rangle = 4 h^{-1} \text{ Mpc}$ is equivalent to decreasing the number of sightlines by an order of magnitude. Thus, comparison of the top center and top right panels of Figure 6 shows that close to the fiducial sightline spacing of $2.5 h^{-1} \text{ Mpc}$, increasing the number of coeval galaxies is more important than increasing the number of background Ly α forest sightlines. However, the measured significance of the signal drops dramatically for sightline spacings $\langle d_{\perp} \rangle > 4 h^{-1} \text{ Mpc}$. This suggests that a wide-field survey such as PFS is preferable for measuring galaxy-cosmic web alignments, as it would be best positioned to deliver a large coeval galaxy sample, while the coarser sightline spacing of $4 h^{-1} \text{ Mpc}$ only modestly lowers the significance compared to the $2.5 h^{-1} \text{ Mpc}$ for CLAMATO. However, the poor performance of the $\langle d_{\perp} \rangle = 6.5 h^{-1} \text{ Mpc}$ survey suggests that constraints on galaxy-cosmic web alignments from PFS will require a supplementary tomography component to achieve the necessary sightline spacing.

The impact of spectroscopic redshift errors are quite modest, as Figure 6 shows little difference between a sample with redshift errors $\sim 100 \text{ km s}^{-1}$ (characteristic of redshifts measured from rest-frame optical nebular emission lines) and a sample with redshift errors $\sim 300 \text{ km s}^{-1}$ (characteristic of redshifts measured from rest-frame UV absorption lines). The impact on the significance is quite small even if the redshifts were from emission lines in a grism spectrum ($\sigma_v \sim 500 \text{ km s}^{-1}$) However, a redshift error of $\sim 2000 \text{ km s}^{-1}$ from the randomized sample leads to a drastic reduction in the constraining power of the survey. Since this redshift error is already optimistic for photometric redshifts, we

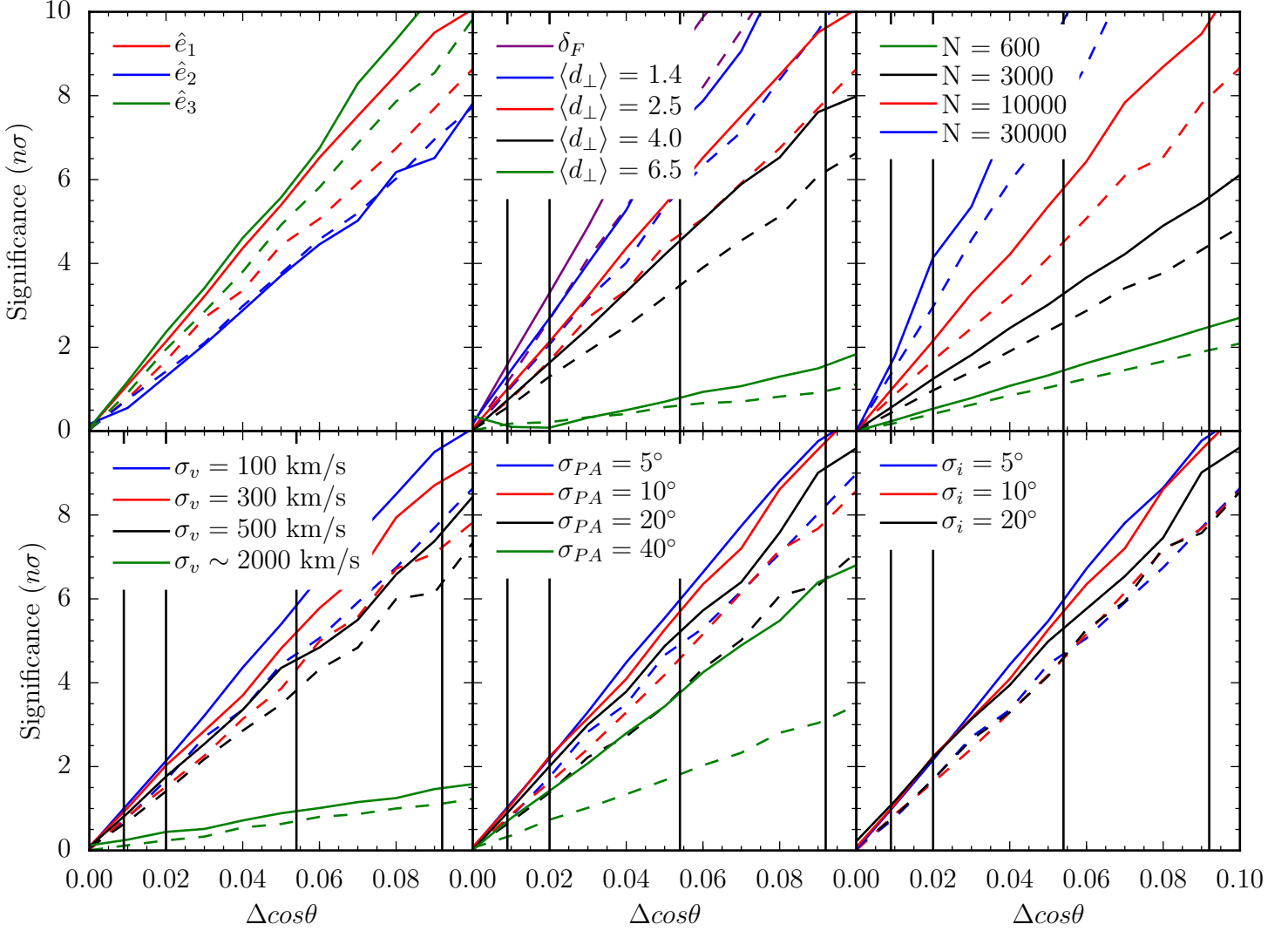


Figure 6. Forecasted significance of the measured galaxy spin-cosmic web alignment as a function of the true alignment between galaxy spins and the cosmic web. The y -axis indicates the significance of the measurement in units of σ , while the x -axis indicates the deviation of the true alignment from random. For all panels except the top left, the galaxy spin axis is misaligned from either \hat{e}_1 , \hat{e}_2 , or \hat{e}_3 . In the top left panel, the galaxy spin axis is misaligned from either \hat{e}_1 , \hat{e}_2 , or \hat{e}_3 . For all panels, the solid lines refer to 3D measurements (alignment between eigenvector and 3D galaxy spin inferred from position angle and ellipticity of the galaxy image) while the dashed lines refer to 2D measurements (alignment between the eigenvector projected in the plane of the sky and the galaxy position angle). Our fiducial survey has $\langle d_{\perp} \rangle = 2.5 h^{-1} \text{ Mpc}$, 10000 galaxies, $\sigma_v = 100 \text{ km s}^{-1}$, $\sigma_{PA} = 10^\circ$, and $\sigma_i = 10^\circ$. In each panel, we vary exactly one of these parameters while keeping the others fixed. *Top left:* Forecasts for alignments between galaxy spin and \hat{e}_1 , \hat{e}_2 and \hat{e}_3 . *Top center:* Forecasts for alignment between galaxy spin and \hat{e}_1 for a variety of IGM tomography surveys with different sightline spacings, including a “perfect” survey where the map is given by δ_F from the simulation. Vertical lines indicate different alignment models from simulations, as defined in Table 2. *Top right:* forecasts for alignment between galaxy spin and \hat{e}_1 for coeval galaxy samples of different sizes. *Bottom left:* Forecasts for alignment between galaxy spin and \hat{e}_1 for different redshift errors. *Bottom center:* Forecasts for alignment between galaxy spin and \hat{e}_1 for different errors in the galaxy position angle. *Bottom right:* Forecasts for alignment between galaxy spin and \hat{e}_1 for different errors in the inclination. Note that changing the inclination error does not affect the 2D measurement because it does not incorporate any information from the inclination.

conclude that spectroscopic redshifts are essential to measure spin-cosmic web alignments.

Varying the fiducial position angle and inclination errors by a factor of two makes relatively little difference for measuring the alignment signal. We also test a model with a relatively large PA error of 40° , which may be more representative of the shape errors in a ground-based survey. In this case, much more of the constraining power is coming from

the inclination. If the survey is also unable to recover the inclinations (due to large uncertainties in measuring the axis ratio), the significance of the alignment signal drops dramatically. Therefore, reasonably precise estimates of the position error ($\sigma_{PA} \lesssim 30^\circ$) will be necessary to measure alignments between galaxy spin and the cosmic web.

We also explore the possibilities for constraining alignment models based on results from simulations. Simula-

tions have measured a broad variety of alignments (e.g. between halo/galaxy spins/shapes and filaments/ \hat{e}_1) across a wide range of redshifts. In general, simulations have found stronger alignments between halo shapes and the cosmic web than between halo spins and the cosmic web (Hahn et al. 2007a). While we have framed the above discussion in terms of galaxy spin alignments, ultimately we are measuring the major axis of the galaxy image, which may be set by either the spin or the shape of the galaxy and ultimately the dark matter halo. Therefore, we consider alignment models from both galaxy spin and halo shape.

We use the simulation results of Hahn et al. (2007a) to create an alignment model based on halo shape. Hahn et al. (2007a) studies the alignment between halo shape and \hat{e}_1 at $z = 0, 0.49, \text{ and } 1.05$. After accounting for the mass dependence by scaling by the mass scale of nonlinear collapse $M_*(z)$ they find no additional redshift dependence.

We extrapolate the results of Hahn et al. (2007a) to $z \sim 2.3$ to create an alignment model. Hahn et al. (2007a) presents the mass dependence of their result using M_h/M_* where M_* is the mass for which a $1\text{-}\sigma$ fluctuation reaches the threshold for spherical collapse, $\delta_c = 1.686$. At $z \sim 2.3$, the typical halo ($M_h \sim 10^{12} M_\odot$) in the galaxy sample has $M \gtrsim 100 M_*$, leading to an extremely strong alignment signal, median $\cos \theta = 0.78$ ($\langle \cos \theta \rangle = 0.73$ assuming the PDF follows Equation 7). More conservatively, it is possible that above $z \sim 1.05$ the alignment signal is constant with M_h rather than M_h/M_* . In this case, the typical halo detected in our galaxy sample would have $M \sim 10 M_{*,z=1.05}$, leading to a slightly weaker median $\cos \theta = 0.7$ ($\langle \cos \theta \rangle = 0.64$) between \hat{e}_1 and halo shape. To translate from halo shape alignments to galaxy shape alignments, we use the halo-galaxy misalignment model of Okumura et al. (2009), a Gaussian distribution of halo-galaxy misalignment angles with dispersion 35° . Therefore, we find $\Delta \langle \cos \theta \rangle = 0.092$ (0.054) for the Hahn et al. (2007a) model using M_h/M_* (M_h) to determine alignments.

In contrast to the shape measurements, several workers have measured alignments between galaxy spins and the cosmic web using hydrodynamic simulations of the galaxies. These include Codis et al. (2015), who measure alignments between galaxy spin and \hat{e}_1 at $z \sim 1.2$, finding $\Delta \langle \cos \theta \rangle = 0.009$. Similarly, Dubois et al. (2014) measure alignments between galaxy spin and filaments for galaxies between $z \sim 1.2$ and $z \sim 3$ and find $\Delta \langle \cos \theta \rangle = 0.02$. These alignments are similar to alignments inferred from simulations of halo spin-cosmic web alignments (Hahn et al. 2007a, Trowland et al. 2013) with a galaxy-halo spin misalignment following Bett (2012). The spin-web alignment is considerably weaker than the shape-web alignment, consistent with results using only dark matter halos (Hahn et al. 2007a) and possibly related to stronger shape-cosmic web alignments for early-type than late-type galaxies observed at low redshift (Tempel & Libeskind 2013, Pahwa et al. 2016) and the considerably stronger intrinsic alignments observed for early-type than late-type galaxies (Joachimi et al. 2013, Mandelbaum et al. 2006).

Figure 6 shows that IGM tomography surveys in tandem

with wide-field galaxy surveys would be able to detect or rule out alignment models based on halo shape (e.g. from Hahn et al. (2007a) at high significance. Even the combination of the CLAMATO survey and zCOSMOS galaxy survey (with $N_{\text{gal}} \sim 600$ over the $V \sim 10^6 h^{-3} \text{Mpc}^3$ CLAMATO volume at $2.1 < z < 2.5$) will be sufficient to detect or rule out the most aggressive alignment models based on halo shape at $\sim 2\text{-}3 \sigma$. However, more realistic models with smaller alignments will require an order of magnitude more coeval galaxies for detection at a similar level. Figure 6 also shows that ground-based imaging should be sufficient to measure galaxy spins as long as position angles can be measured with an error $\lesssim 20^\circ$.

Additional measurements besides spin-eigendirection correlations may yield further independent information. For instance, IGM tomography will be able to identify a large number of voids (Stark et al. 2015a), allowing measurement of the void-spin correlation (e.g. Trujillo et al. 2006, Slosar & White 2009, Varela et al. 2012). We can also use the eigenvalues to partition our map into voids, sheets, filaments, and nodes (Lee & White 2016) and measure spin- \hat{e}_1 alignments only in filaments, or spin- \hat{e}_3 alignments only in sheets, where they may be strongest (e.g. Hahn et al. 2007a).

4. CONCLUSIONS

Intrinsic alignments between galaxies and the underlying cosmic web have been predicted from both DM-only and hydrodynamical simulations, several of which predict increasing alignment strength at higher redshift ($z \gtrsim 1$). At these redshifts, it becomes increasingly expensive to obtain spectroscopic redshifts with sufficiently high number densities to trace the cosmic web. Recently, tomographic reconstruction of the IGM as traced by high area densities of Lyman- α forest sightlines has emerged as a promising method to map the cosmic web at $z \sim 2 - 3$.

In this paper, we studied the feasibility of IGM tomographic surveys, in conjunction with coeval galaxy redshift samples with measured structural parameters, to place constraints on galaxy-cosmic web alignments at $z \sim 2.5$. Using detailed hydrodynamical simulations based on the Nyx code, we first generated realistic mock data sets reflecting both ongoing and future IGM tomography surveys. The galaxy spin or shape distributions were ‘painted on’ with respect to the underlying matter tidal tensor field using a simple alignment model parameterized by $\Delta \langle \cos \theta \rangle$, i.e. the non-random excess alignment of the galaxies with respect to the eigenvectors of the matter tidal tensor. Future studies of galaxy-cosmic web alignments at $z \sim 2$ will benefit greatly from simulations combining both realistic IGM physics and galaxy formation (e.g. future versions of the Nyx simulations used in this paper).

First, we showed that IGM tomography with sightline separations of $\langle d_\perp \rangle \leq 5 h^{-1} \text{Mpc}$ should be able to recover the eigenvectors of the tidal tensor, \hat{e}_1 , \hat{e}_2 , and \hat{e}_3 , as determined from the large-scale distribution of matter in the universe (smoothed on $2 h^{-1} \text{Mpc}$ scales). The mean dot products between the eigenvectors as determined by the matter field and the eigenvectors from a mock observation with sight-

line spacing $2.5 h^{-1}$ Mpc, similar to the ongoing CLAMATO survey, are $[0.815, 0.722, 0.838]$ for $[\hat{e}_1, \hat{e}_2, \hat{e}_3]$. This builds on our previous result showing that IGM tomography can recover eigenvalue cosmic web classifications with a fidelity similar to $z \lesssim 0.7$ surveys (Lee & White 2016).

We then compared the eigenvectors recovered from the IGM tomography with the spins or shapes in coeval galaxy samples as a function of the alignment strength $\Delta\langle\cos\theta\rangle$, and also considered the effect of uncertainties in the measurement of the galaxy position angles, inclinations, and redshift estimation. The largest factor in our ability to constrain the galaxy-cosmic web alignments is the size of the galaxy sample. Assuming a fiducial mean sightline separation of $\langle d_{\perp}\rangle = 2.5 h^{-1}$ Mpc, redshift errors of $\sigma_v = 500 \text{ km s}^{-1}$, as well as errors of $\sigma_{\text{PA}} = 10 \text{ deg}$ and $\sigma_i = 10 \text{ deg}$ in the galaxy position angles and inclinations, respectively, we find that the ongoing CLAMATO Survey on the Keck-I Telescope⁵, in conjunction with ~ 600 coeval galaxies from zCOSMOS-Deep and other spectroscopic surveys, should be able to place $\sim 3\sigma$ limits on the most extreme alignment models with $\Delta\langle\cos\theta\rangle \sim 0.1$ within the next few years. For most alignment models with $\Delta\langle\cos\theta\rangle < 0.05$, however, coeval samples of at least several thousand galaxies with spectroscopic redshifts would be needed to make a $\sim 3 - 4\sigma$ detection. These results are not very sensitive to the mean sightline separation of the IGM tomography survey so long as $\langle d_{\perp}\rangle \lesssim 5 h^{-1}$ Mpc, nor on the accuracy of the galaxy structural parameters, although space-based imaging or very good quality ground-based imaging (< 0.5 arcsec seeing) would be desirable for the latter. We find that photometric redshifts are insufficient for this purpose as the redshift errors are far too large.

Since the primary limitation for this alignment measurement is the size of available galaxy redshift samples at $z \sim 2.5$, a relatively wide/shallow strategy would be optimal: at fixed survey magnitude, the galaxy sample size N_{gal} scales linearly with telescope time by expanding survey area. On the other hand, increasing N_{gal} by increasing survey depth within a small survey area would require exponential increases of telescope time. Since the tidal tensor eigenvector recovery does not degrade much with slightly coarser tomographic reconstructions relative to the fiducial $2.5 h^{-1}$ Mpc sightline spacing in CLAMATO, this argues

that near-future wide-field instruments, i.e. Subaru PFS, can cover much larger areas than CLAMATO with the concomitantly larger N_{gal} for significantly improved spin-cosmic web or shape-cosmic web constraints. However, we did find a mean spacing of $\langle d_{\perp}\rangle < 5 h^{-1}$ Mpc is required for the Ly α forest sightlines, above which the eigenvector recovery degrades considerably. Since the $2 < z < 3$ LBG component currently planned for the $\sim 20 - 30$ sq deg PFS Galaxy Evolution Survey leads to a “free” IGM tomographic map with $\langle d_{\perp}\rangle \sim 6.5 h^{-1}$ Mpc, we advocate supplemental PFS spectroscopy to boost the sightline sampling to $\langle d_{\perp}\rangle \approx 4 h^{-1}$ Mpc. Based on the calculations of Lee et al. (2014a), this should require $\sim 5 - 6$ hrs of additional exposure time per field, or ~ 20 nights over ~ 25 sq deg (including weather/seeing overheads). Such a program, along with the $\sim 10,000$ coeval galaxies also from PFS, should allow 3σ limits on alignments down to $\Delta\langle\cos\theta\rangle \approx 0.03$. Constraints on even smaller $\Delta\langle\cos\theta\rangle$, at the levels predicted by, e.g. Codis et al. (2015), would require even more ambitious surveys. However, it is conceivable that a new generation of massively-multiplexed wide-field spectrographs on $>10\text{m}$ -class telescopes could be available by the early 2030s (McConnachie et al. 2016, Dodelson et al. 2016, Najita et al. 2016), in time to provide priors on the intrinsic alignment systematics for the final LSST tomographic weak lensing analyses.

We thank Peter Nugent, Miguel Aragon-Calvo, Nadia Zalkamska, Joanne Cohn, and Sedona Price for useful discussions and comments. K.G.L. acknowledges support for this work by NASA through Hubble Fellowship grant HF2-51361 awarded by the Space Telescope Science Institute, which is operated by the Association of Universities for Research in Astronomy, Inc., for NASA, under contract NAS5-26555. ZL and AK were in part supported by the Scientific Discovery through Advanced Computing (SciDAC) program funded by U.S. Department of Energy Office of Advanced Scientific Computing Research and the Office of High Energy Physics. Calculations presented in this paper used resources of the National Energy Research Scientific Computing Center (NERSC), which is supported by the Office of Science of the U.S. Department of Energy under Contract No. DE-AC02-05CH11231.

REFERENCES

- Adelberger, K. L., Shapley, A. E., Steidel, C. C., et al. 2005, *ApJ*, **629**, 636
 Almgren, A. S., Bell, J. B., Lijewski, M. J., Lukić, Z., & Van Andel, E. 2013, *ApJ*, **765**, 39
 Alpaslan, M., Driver, S., Robotham, A. S. G., et al. 2015, *MNRAS*, **451**, 3249
 Altay, G., Colberg, J. M., & Croft, R. A. C. 2006, *MNRAS*, **370**, 1422
 Aragón-Calvo, M. A., van de Weygaert, R., Jones, B. J. T., & van der Hulst, J. M. 2007, *ApJ*, **655**, L5
 Aragón-Calvo, M. A., & Yang, L. F. 2014, *MNRAS*, **440**, L46
 Bett, P. 2012, *MNRAS*, **420**, 3303
 Bond, J. R., Kofman, L., & Pogosyan, D. 1996, *Nature*, **380**, 603
 Bridle, S., & King, L. 2007, *New Journal of Physics*, **9**, 444
 Brunino, R., Trujillo, I., Pearce, F. R., & Thomas, P. A. 2007, *MNRAS*, **375**, 184
 Caucci, S., Colombi, S., Pichon, C., et al. 2008, *MNRAS*, **386**, 211
 Cautun, M., van de Weygaert, R., Jones, B. J. T., & Frenk, C. S. 2014, *MNRAS*, **441**, 2923
 Chang, Y.-Y., van der Wel, A., Rix, H.-W., et al. 2013, *ApJ*, **762**, 83
 Chen, Y.-C., Ho, S., Tenneti, A., et al. 2015, *MNRAS*, **454**, 3341
 Codis, S., Pichon, C., Devriendt, J., et al. 2012, *MNRAS*, **427**, 3320
 Codis, S., Gavazzi, R., Dubois, Y., et al. 2015, *MNRAS*, **448**, 3391

⁵ Comoving volume of $V \sim 10^6 h^{-3} \text{ Mpc}^3$ over $2.1 < z < 2.5$ within the central square degree of the COSMOS Field.

- Cuesta, A. J., Betancort-Rijo, J. E., Gottlöber, S., et al. 2008, *MNRAS*, **385**, 867
- Davis, M., Efstathiou, G., Frenk, C. S., & White, S. D. M. 1985, *ApJ*, **292**, 371
- Diener, C., Lilly, S. J., Knobel, C., et al. 2013, *ApJ*, **765**, 109
- Diener, C., Lilly, S. J., Ledoux, C., et al. 2015, *ApJ*, **802**, 31
- Dodelson, S., Heitmann, K., Hirata, C., et al. 2016, ArXiv e-prints, [arXiv:1604.07626](https://arxiv.org/abs/1604.07626)
- Doroshkevich, A. G. 1970, *Astrofizika*, **6**, 581
- Dubois, Y., Pichon, C., Welker, C., et al. 2014, *MNRAS*, **444**, 1453
- Eardley, E., Peacock, J. A., McNaught-Roberts, T., et al. 2015, *MNRAS*, **448**, 3665
- Einasto, J., Klypin, A. A., Saar, E., & Shandarin, S. F. 1984, *MNRAS*, **206**, 529
- Forero-Romero, J. E., Contreras, S., & Padilla, N. 2014, *MNRAS*, **443**, 1090
- Forero-Romero, J. E., Hoffman, Y., Gottlöber, S., Klypin, A., & Yepes, G. 2009, *MNRAS*, **396**, 1815
- Franx, M., Illingworth, G., & de Zeeuw, T. 1991, *ApJ*, **383**, 112
- Geller, M. J., & Huchra, J. P. 1989, *Science*, **246**, 897
- Giardino, G., de Oliveira, C. A., Arribas, S., et al. 2016, in *Astronomical Society of the Pacific Conference Series*, Vol. 507, Multi-Object Spectroscopy in the Next Decade: Big Questions, Large Surveys, and Wide Fields, ed. I. Skillen, M. Barcellis, & S. Trager, 305
- Giavalisco, M., Steidel, C. C., & Macchetto, F. D. 1996, *ApJ*, **470**, 189
- Guzzo, L., Scodreggio, M., Garilli, B., et al. 2014, *A&A*, **566**, A108
- Haardt, F., & Madau, P. 2012, *ApJ*, **746**, 125
- Hahn, O., Carollo, C. M., Porciani, C., & Dekel, A. 2007a, *MNRAS*, **381**, 41
- Hahn, O., Porciani, C., Carollo, C. M., & Dekel, A. 2007b, *MNRAS*, **375**, 489
- Hahn, O., Teyssier, R., & Carollo, C. M. 2010, *MNRAS*, **405**, 274
- Haynes, M. P., & Giovanelli, R. 1984, *AJ*, **89**, 758
- Hirata, C. M., & Seljak, U. 2004, *Phys. Rev. D*, **70**, 63526
- Joachimi, B., Semboloni, E., Bett, P. E., et al. 2013, *MNRAS*, **431**, 477
- Jones, B. J. T., van de Weygaert, R., & Aragon-Calvo, M. A. 2010, *MNRAS*, **408**, 897
- Kiessling, A., Cacciato, M., Joachimi, B., et al. 2015, *Space Sci. Rev.*, **193**, 67
- Kirk, D., Rassat, A., Host, O., & Bridle, S. 2012, *MNRAS*, **424**, 1647
- Klypin, A. A., & Shandarin, S. F. 1983, *MNRAS*, **204**, 891
- Kriek, M., Shapley, A. E., Reddy, N. A., et al. 2015, *ApJs*, **218**, 15
- Law, D. R., Shapley, A. E., Steidel, C. C., et al. 2012, *Nature*, **487**, 338
- Leauthaud, A., Massey, R., Kneib, J.-P., et al. 2007, *ApJs*, **172**, 219
- Lee, J., & Erdogdu, P. 2007, *ApJ*, **671**, 1248
- Lee, J., & Pen, U.-L. 2000, *ApJL*, **532**, L5
- , 2001, *ApJ*, **555**, 106
- Lee, J., & Pen, U.-L. 2002, *ApJL*, **567**, L111
- Lee, J., & Pen, U.-L. 2007, *ApJL*, **670**, L1
- Lee, K.-G., Hennawi, J. F., White, M., Croft, R. A. C., & Ozbek, M. 2014a, *ApJ*, **788**, 49
- Lee, K.-G., Suzuki, N., & Spergel, D. N. 2012, *AJ*, **143**, 51
- Lee, K.-G., & White, M. 2016, *ArXiv e-prints*
- Lee, K.-G., Hennawi, J. F., Stark, C., et al. 2014b, *ApJL*, **795**, L12
- Lee, K.-G., Hennawi, J. F., White, M., et al. 2016, *ApJ*, **817**, 160
- Libeskind, N. I., Hoffman, Y., Forero-Romero, J., et al. 2013, *MNRAS*, **428**, 2489
- Lilly, S. J., Le Fèvre, O., Renzini, A., et al. 2007, *ApJs*, **172**, 70
- Lotz, J. M., Madau, P., Giavalisco, M., Primack, J., & Ferguson, H. C. 2006, *ApJ*, **636**, 592
- LSST Science Collaboration, Abell, P. A., Allison, J., et al. 2009, ArXiv e-prints, [arXiv:0912.0201](https://arxiv.org/abs/0912.0201) [[astro-ph.IM](https://arxiv.org/abs/0912.0201)]
- Lukić, Z., Stark, C. W., Nugent, P., et al. 2015, *MNRAS*, **446**, 3697
- Malavasi, N., Arnouts, S., Vibert, D., et al. 2016, ArXiv e-prints, [arXiv:1611.07045](https://arxiv.org/abs/1611.07045)
- Mandelbaum, R., Hirata, C. M., Ishak, M., Seljak, U., & Brinkmann, J. 2006, *MNRAS*, **367**, 611
- McConnachie, A., Babusiaux, C., Balogh, M., et al. 2016, ArXiv e-prints, [arXiv:1606.00043](https://arxiv.org/abs/1606.00043) [[astro-ph.IM](https://arxiv.org/abs/1606.00043)]
- Momcheva, I. G., Brammer, G. B., van Dokkum, P. G., et al. 2016, *ApJs*, **225**, 27
- Najita, J., Willman, B., Finkbeiner, D. P., et al. 2016, ArXiv e-prints, [arXiv:1610.01661](https://arxiv.org/abs/1610.01661) [[astro-ph.IM](https://arxiv.org/abs/1610.01661)]
- Navarro, J. F., Abadi, M. G., & Steinmetz, M. 2004, *ApJ*, **613**, 41
- Okumura, T., Jing, Y. P., & Li, C. 2009, *ApJ*, **694**, 214
- Pahwa, I., Libeskind, N. I., Tempel, E., et al. 2016, *MNRAS*, **457**, 695
- Patiri, S. G., Cuesta, A. J., Prada, F., Betancort-Rijo, J., & Klypin, A. 2006, *ApJL*, **652**, L75
- Peebles, P. J. E. 1969, *ApJ*, **155**, 393
- Pichon, C., Vergely, J. L., Rollinde, E., Colombi, S., & Petitjean, P. 2001, *MNRAS*, **326**, 597
- Planck Collaboration, Adam, R., Ade, P. A. R., et al. 2016, *A&A*, **594**, A1
- Porciani, C., Dekel, A., & Hoffman, Y. 2002, *MNRAS*, **332**, 325
- Rakic, O., Schaye, J., Steidel, C. C., & Rudie, G. C. 2012, *ApJ*, **751**, 94
- Schmittfull, M., & White, M. 2016, *MNRAS*, **463**, 332
- Scoville, N., Aussel, H., Brusa, M., et al. 2007, *ApJs*, **172**, 1
- Slosar, A., & White, M. 2009, *JCAP*, **6**, 9
- Stark, C. W., Font-Ribera, A., White, M., & Lee, K.-G. 2015a, *MNRAS*, **453**, 4311
- Stark, C. W., White, M., Lee, K.-G., & Hennawi, J. F. 2015b, *MNRAS*, **453**, 311
- Steidel, C. C., Erb, D. K., Shapley, A. E., et al. 2010, *ApJ*, **717**, 289
- Takada, M., Ellis, R. S., Chiba, M., et al. 2014, *PASJ*, **66**, R1
- Tempel, E., & Libeskind, N. I. 2013, *ApJL*, **775**, L42
- Tempel, E., Stoica, R. S., & Saar, E. 2013, *MNRAS*, **428**, 1827
- Trowland, H. E., Lewis, G. F., & Bland-Hawthorn, J. 2013, *ApJ*, **762**, 72
- Trujillo, I., Carretero, C., & Patiri, S. G. 2006, *ApJL*, **640**, L111
- Van Der Wel, A., Bell, E. F., Häussler, B., et al. 2012, *ApJs*, **203**, 24
- Van Der Wel, A., Franx, M., Van Dokkum, P. G., et al. 2014, *ApJ*, **788**, 28
- Varela, J., Betancort-Rijo, J., Trujillo, I., & Ricciardelli, E. 2012, *ApJ*, **744**, 82
- Viel, M., Schaye, J., & Booth, C. M. 2013, *MNRAS*, **429**, 1734
- White, S. D. M. 1984, *ApJ*, **286**, 38
- Wilson, M. J., Peacock, J. A., Taylor, A. N., & de la Torre, S. 2015, ArXiv e-prints, [arXiv:1511.07799](https://arxiv.org/abs/1511.07799)
- Wisnioski, E., Förster Schreiber, N. M., Wuyts, S., et al. 2015, *ApJ*, **799**, 209
- Zeldovich, I. B., Einasto, J., & Shandarin, S. F. 1982, *Nature*, **300**, 407
- Zel'dovich, Y. B. 1970, *A&A*, **5**, 84
- Zhang, Y., Yang, X., Faltenbacher, A., et al. 2009, *ApJ*, **706**, 747
- Zhang, Y., Yang, X., Wang, H., et al. 2015, *ApJ*, **798**, 17
- , 2013, *ApJ*, **779**, 160